International Journal of Fatigue 216 (2027) 110076

Contents lists available at ScienceDirect

International Journal of Fatigue

journal homepage: www.elsevier.com/locate/ijfatigue

Numerical fatigue life prediction by adapting novel short-time evaluation procedures to microstructure-sensitive fatigue modeling

Christian Häffner [a,*], Niklas C. Fehlemann [a], Sophie C. Stebner [a], Felix Weber [b], Sebastian Münstermann [a]

[a] Institute of Metal Forming, RWTH Aachen University, Aachen, 52072, Germany
[b] Institute for Materials Applications in Mechanical Engineering, RWTH Aachen University, Aachen, 52062, Germany

ARTICLE INFO

Keywords:
Crystal plasticity finite element method
Short-time evaluation procedure
Representative volume element
Low cycle fatigue
Fatigue modeling

ABSTRACT

Structures and components in a wide variety of industries must withstand cyclic loads over an extended period of time. If failure occurs due to material fatigue, far-reaching consequences may entail. Accordingly, knowledge of the material's fatigue life is essential. Since determining the relevant material properties in terms of Wöhler or strain-life curves requires significant experimental effort, numerous studies in the literature focus on accelerated lifetime prediction using so-called short-time evaluation procedures. In this article, such short-time evaluation procedures are adapted for the first time to the numerical framework of microstructure-sensitive fatigue modeling. Micromechanically motivated fatigue indicator parameters calculated by a crystal plasticity motivated material model serve as the numerical surrogate of the material's response, which is otherwise derived from experiments. By applying boundary conditions of a strain increase test to multiple statistically representative volume elements of the underlying microstructure, the incremental cyclic damage at each load level can be calculated from the fatigue indicator parameters. Using these damage values, virtual lifetimes can then be calculated based on the damage accumulation in analogy to Palmgren-Miner. The numerically determined fatigue lives, based on the two fatigue indicator parameters – accumulated plastic strain and strain energy density – show good agreement with experimental results. The material under investigation in this study is an austenitic stainless steel of grade AISI 347, often used in nuclear power plant components.

1. Introduction

Since many structures and components in aviation, mobility, and power plants are subjected to recurring, cyclic loads during operation, knowledge of the cyclic material properties and fatigue life – represented by Wöhler (S-N) or strain-life (ε-N) curves – is of particular importance. These curves are usually generated through extensive experimentation, which demands considerable time and resources. For example, the German standard DIN EN 6072 [1] specifies that at least 10 valid fatigue tests are required to generate S-N curves. According to the current draft of the international standard ISO/DIS 12016 [2], only eight tests are required for generating ε-N curves, whose number of cycles to failure, however, must cover at least three decades. Contrary, the American standard ASTM E606/E606M [3] requires at least 10 tests for a single ε-N curve. Since all of these are however minimum requirements, significantly more tests are often conducted to ensure statistical validity of the results, e.g., Koller et al. [4], Scholl et al. [5] or Stopka and Sangid [6].

In order to cover the whole regime of the finite fatigue life, multiple constant amplitude tests have to be performed over a wide range of load levels, which is not only very time expensive, but also very costly. To tackle these issues, so-called short-time evaluation procedures have been developed over the past decade and are still being developed today. Using these experimental, accelerated lifetime prediction methods, S-N as well as ε-N curves can be obtained quickly with minimal material and time consumption. For example, *PHYBAL* [7] based approaches such as *StressLife* [8,9] or *StrainLife* [10,11] require only two constant amplitude tests in addition to a single load increase test or strain increase test, respectively. To further reduce the experimental effort, Weber et al. [12] recently introduced the *MiDAcLife* approach, which allows S-N curves in the high cycle fatigue (HCF) regime to be predicted using just a single load increase test. By calculating the incremental cyclic damage on each load level, adapting the linear damage accumulation by Palmgren-Miner [13,14], virtual number of cycles to failure and hence Wöhler curves can be determined with minimal effort. While Weber et al. [12] introduced this concept to a

* Corresponding author.
E-mail address: christian.haeffner@ibf.rwth-aachen.de (C. Häffner).

https://doi.org/10.1016/j.ijfatigue.2026.110076
Received 20 August 2026; Received in revised form 9 October 2026; Accepted 3 November 2026
Available online 10 November 2026
0142-1123/© 2026 The Authors. Published by Elsevier Ltd. This is an open access article under the CC BY license (http://creativecommons.org/licenses/by/4.0/).
Open access funding enabled and organized by Projekt DEAL.

ferritic-bainitic steel of type 20MnMoNi5-5 (1.6310), in the same work they further validated their methodology on SAE 1020, SAE 1045 and SAE 5120 steel. Additionally, Weber et al. [15] successfully applied this approach to heavy-section castings made from ADI grade 2. While *MiDAcLife* [12] can be used to calculate virtual lifetimes for stress-controlled fatigue tests in the HCF regime, in previous work [16], the authors recently adopted this approach to predict the low cycle fatigue (LCF) regime under total strain control for a metastable austenitic stainless steel of type AISI 347, titled *MiDAcStrain*.

What these approaches have in common is that they aim to obtain a large amount of information from as few specimens as possible. In this context, the material's response is recorded during the tests and serves as input for the corresponding lifetime prediction method. While non-destructive testing-based parameters such as the tangential magnetic field strength ΔM_{tang}, the electrical circuit potential ΔE_{CP}, the electrical resistance ΔR or the change in temperature ΔT can be used as the material's response M, the stress amplitude σ_{a} can also be used as the material's response in the simplest case [10,11,17,18].

For the accelerated lifetime prediction, both *MiDAcLife* [12] and *MiDAcStrain* [16] rely on load and strain increase tests, respectively. Recently, however, Koch et al. [19] presented an approach for calculating S-N curves in the HCF regime by performing only a single constant amplitude test, named *Hysteresis-Life*, which they successfully applied to two different aluminum alloys, EN AW-6060 and EN AW-6082-T6.

However, it must be noted that while these short-time evaluation procedures aim to provide S-N and ε-N curves quickly – and thus in a time- and cost-efficient manner – they yield only trend curves. Due to the small number of tests, it is not possible to apply probabilistic methods and, consequently, to calculate failure or survival probabilities. This indeed limits the applicability of these methods to the practical fatigue design of real components. However, due to the rapid generation of trend curves, these methods are ideally suited for rapid material screening and an initial estimation of fatigue life, for example, in the field of quality assurance.

As was shown, much effort is put into the experimental development of accelerated lifetime prediction methods. However, with computational power becoming more available and accessible, researchers worldwide are further focusing on computational methods enabling to determine cyclic material properties, without the need for extensive experimentation. These approaches can be separated into data-driven methods and simulation-based approaches. Using data-driven methods, stress intensity factors [20,21], crack propagation [22–24] as well as fatigue lifetimes [25–28] can be predicted with high accuracy. Data-driven approaches, however, require a substantial amount of data available for training and testing. An overview of machine-learning-based fatigue life predictions for metallic materials is given by Wang et al. [29].

The underlying microstructure of a material significantly influences the mechanical properties and, consequently, the cyclic material properties as well as the fatigue life. Hence, within the concept of microstructure-sensitive fatigue modeling as introduced by McDowell and Dunne [30], the microstructure is taken into account in the form of so-called SRVEs in combination with crystal plasticity motivated constitutive models. In addition to the classical finite element method (FEM), fast Fourier transform (FFT) solvers are also available, as shown, for example, in [31–34]. On top of that, crystal plasticity models in conjunction with phase field approaches are also becoming more popular, especially in predicting crack paths [35,36].

When predicting fatigue life within the microstructure-sensitive fatigue modeling approach, so-called FIPs are often used as a surrogate for fatigue crack initiation. Further details on FIPs are provided in Section 3.3. From these FIPs, the fatigue life in terms of number of cycles to failure can be calculated. However, there exist different mathematical approaches to calculate the respective number of cycles to failure N_{sim}. In general, often a power law relation following Cruzado et al. [37] as

$$N_{\mathrm{sim,i}} = \frac{FIP_{\mathrm{crit}}}{\left(\Delta FIP_i\right)^p} \tag{1}$$

is adapted, with the index i denoting a single SRVE simulation at a defined load amplitude. ΔFIP represents the saturated FIP increment and hence the slope of the FIP evolution, which can often be linearly approximated. FIP_{crit} and p, however, serve as material parameters, which have to be calibrated against experimental results. When setting $p = 1$, a linear model is given as used, for example, by Manonukul and Dunne [38] and Boeff et al. [39]. Inspired by the work of Mughrabi [40,41], both Sayer et al. [42] and He et al. [43] incorporated the reversibility of cyclic slip into their respective FIP definition and lifetime calculation scheme, resulting in

$$N_{\mathrm{sim,i}} = \left(\frac{4\varepsilon_{\mathrm{f}}' 2^c}{FIP_{\mathrm{irr,crit}}\,\Delta FIP_i} \right)^{-\frac{1}{c}} \tag{2}$$

Here $\varepsilon_{\mathrm{f}}'$ and c are experimentally determined parameters of the Coffin-Manson-Basquin relation [44–46] and $FIP_{\mathrm{irr,crit}}$ denotes the new critical FIP, taking into account the slip irreversibility.

As can be seen from Eqs. (1) and (2), several parameters have to be determined to predict the fatigue life over a wide range of load amplitudes. Additionally, these equations only allow to calculate the fatigue life for a single SRVE at a specific load level, indicated by the index i, mimicking a constant amplitude test. Hence, multiple simulations have to be performed over a wide range of load amplitudes to cover a whole S-N or ε-N curve. While experimental effort can be reduced substantially – down to a single load or strain increase test – the research question remains whether these experimental short-time evaluation procedures can be transferred to computational approaches, in particular microstructure-sensitive fatigue modeling.

The aim of the present study is therefore to answer this question by adapting the *MiDAcStrain* approach, presented in previous work [16], within the framework of microstructure-sensitive fatigue modeling. Strain increase test simulations are performed on multiple SRVEs, extracting two different FIPs as a numerical surrogate of the material's response. Based on the respective FIP evolution, incremental cyclic damage is calculated on each load level, which serves as the foundation for predicting virtual lifetimes. For statistical validation, in total 20 SRVE simulations are performed. The proposed concept is validated against experimental constant amplitude tests and strain-life curves in the LCF regime for an austenitic stainless steel grade AISI 347.

This article is structured as follows: Section 2 introduces the material under investigation in terms of microstructure characterization and elaborates on the experimental setup to determine the fatigue life within the LCF regime. Section 3 describes the concept of microstructure-sensitive fatigue modeling, including the generation of SRVEs, the constitutive model based on crystal plasticity theory, as well as the concept of FIPs and the adapted short-time evaluation procedure. The achieved results are shown and discussed in Section 4 and Section 5, respectively. Finally, conclusions are presented in Section 6.

2. Material and experimental setup

The following section presents the material under investigation as well as the experimental setups to characterize the material in detail. Here, the emphasis is on the quantitative characterization of the underlying microstructure through EBSD as this serves as the foundation for the generation of SRVEs. Additionally, the experimental characterization of the fatigue life in the LCF regime is summarized.

Table 1
Chemical composition of AISI 347.

Element	C	Si	Mn	P	S	Co	Cr	Nb	Ni
wt.-%	0.01	0.49	1.28	0.024	0.002	0.14	17.15	0.27	9.27

2.1. Material

The material under investigation is a metastable austenitic stainless steel of type AISI 347. This corresponds to the German designations 1.4550 and X6CrNiNb18-10 according to [47,48]. Here, the addition of Nb prevents intergranular corrosion, which is why this steel grade is classified as a stabilized austenitic stainless steel. Due to its excellent mechanical properties, i.e., high toughness, ductility, and corrosion resistance, this steel is frequently used in the construction of chemical plants and, in particular, nuclear power plants. For example, the guideline KTA 3201.1 [49] of the German Reactor Safety Commission (Kerntechnischer Ausschuss, KTA) approves this material for the construction of pressure retaining components of the reactor coolant pressure boundary of German light water reactors. The chemical composition of the industrially produced steel examined in this study was analyzed using optical emission spectroscopy and is listed in Table 1.

In addition to determining the chemical composition, the microstructure was also characterized using EBSD. For this purpose, a sample was cut from the longitudinal plane of the round bar using wire electrical discharge machining. In addition to mechanical grinding and polishing, the specimen was also subjected to electrolytic polishing, which allowed the deformation-induced martensite on the surface to be removed. The EBSD analysis was conducted in a scanning electron microscope of type Thermofischer Scientific Helios 5 Hydra UX with a working distance of 20 mm and a step size of 0.75 µm in x- and y-direction, respectively. In total, an area of 925 µm × 580 µm was investigated and 19 721 grains were indexed. The raw data was subsequently analyzed using the MATLAB Toolbox MTEX [50,51]. In this step, the grain boundaries were reconstructed by adapting a threshold misorientation angle of 15°. Fig. 1(a) shows the phases present in the microstructure. It can be seen that, despite electrolytic polishing, small amounts of martensite are present in the microstructure. However, since the martensitic phase content is less than 1 %, it can be assumed that this can be removed by adjusting the parameters in the electrolytic polishing step and that the material is therefore fully austenitic in its initial state. By measuring the ferromagnetic content using a FERITSCOPE® DMP® 30, the assumption of a fully austenitic microstructure could be confirmed. Hence, the initial martensite was neglected in the later SRVE generation step.

In addition to the phase composition, the crystallographic orientation of the austenite grains was also characterized. The mean grain orientation is shown in Fig. 1(b) for the region of interest indicated by a black square in Fig. 1(a). It is evident that there is no preferred orientation, and the texture can therefore be considered as random. All indexed austenite grains were then fitted using ellipses [52]. In addition to the grain orientation, consisting of the three Bunge Euler angles (φ_1, Φ, φ_2), the grain area, as well as the two elliptical semi-axes and the inclination angle for each grain, were also extracted. From the lengths of the two elliptical semi-axes, the aspect ratio was calculated, which describes the grain elongation or roundness. The multivariate distribution function for grain area, aspect ratio, inclination angle, and the Bunge Euler angles, as well as their interdependencies, serves as the foundation for generating the SRVEs.

2.2. Fatigue testing

In previous work [16] several constant amplitude tests were performed to characterize the cyclic material behavior and hence the fatigue life in the LCF regime. All constant amplitude tests were conducted on a servo-hydraulic testing setup with a maximum load of 160 kN at room temperature under total strain control with a loading ratio of $R_\varepsilon = -1$. This resulted in equal tension and compression loading and hence a mean strain amplitude of $\varepsilon_{a,m} = 0\,\%$. A constant strain rate of $\dot{\varepsilon} = 0.4\,\%\,s^{-1}$ with a triangular waveform was applied for all constant amplitude tests. Depending on the total strain amplitude, the frequency f was adjusted to guarantee a constant strain rate throughout all fatigue tests.

In addition to the aforementioned constant amplitude tests, a strain increase test was also conducted. This strain increase test forms the foundation of the short-time evaluation *StrainLife*, which has already been successfully applied and validated by several authors for the same metastable austenitic stainless steel grade AISI 347 [10,11,17,18]. The goal of *StrainLife* is the time- and cost-efficient determination of the fatigue life in the LCF regime described by the Coffin-Manson-Basquin equation [44–46] given as follows:

$$\begin{aligned}\varepsilon_{a,t} &= \frac{\sigma_f'}{E}\cdot(2N_f)^b + \varepsilon_f'\cdot(2N_f)^c \\ &= B\cdot(2N_f)^b + C\cdot(2N_f)^c\end{aligned} \tag{3}$$

where σ_f' denotes the fatigue strength coefficient, E the Young's modulus, $2N_f$ the number of reversals to failure, b the fatigue strength exponent, ε_f' the fatigue ductility coefficient and c the fatigue ductility exponent. Even though the Coffin-Manson-Basquin approach is famously lacking an asymptotic definition of the endurance fatigue strength, it is still widely used by researchers, e.g., [10,11,17,18] and is also given in fatigue testing standards [2,3] to describe and evaluate the ε-N curve within the LCF regime up to approximately 100 000 cycles.

Unlike conventional methods, which require a large number of fatigue tests, the *StrainLife* [10] approach requires only a single strain increase test and at least two additional constant amplitude tests to be performed. The boundary conditions for the strain increase test were identical to the ones presented for the uniaxial constant amplitude tests. Due to the constant strain rate and the requirement that a constant total strain be accumulated per strain level in the strain increase test, both the frequency f as well as the number of cycles per strain level n_i had to be reduced. The latter is shown in Eq. (2) as presented by Donnerbauer et al. [18].

$$n_i = \frac{\Delta t\cdot\dot{\varepsilon}}{4\varepsilon_{a,t,i}} = \frac{\varepsilon_{sl}}{\varepsilon_i} \tag{4}$$

Here $\Delta t = 1800\,s$ describes the time spent on each strain level, $\dot{\varepsilon}$ is the total strain rate, and $\varepsilon_{a,t,i}$ is the total strain amplitude at strain level i. This corresponds to the ratio of the total accumulated strain per strain level ε_{sl} to the total strain applied in one single cycle ε_i. For additional details of the experimental setup, the evaluation according to the *StrainLife* approach, as well as the results reused in this study for comparison, the reader is referred to previous work [16].

3. Microstructure-sensitive fatigue modeling

The methodological approach for predicting the finite fatigue life is based on the concept of microstructure-sensitive fatigue modeling introduced by McDowell and Dunne [30]. The two key components of this method are the representation of the microstructure in the form of SRVEs and the numerical description of the phenomena occurring at the microscale using a suitable micromechanically motivated material model in the context of crystal plasticity finite element method (CPFEM). Both are briefly presented in the following sections. Furthermore, the approach of FIPs and their role within the simulation framework, followed by the newly proposed numerical lifetime prediction method *MiDAcStrain*$_{CPFEM}$ are presented.

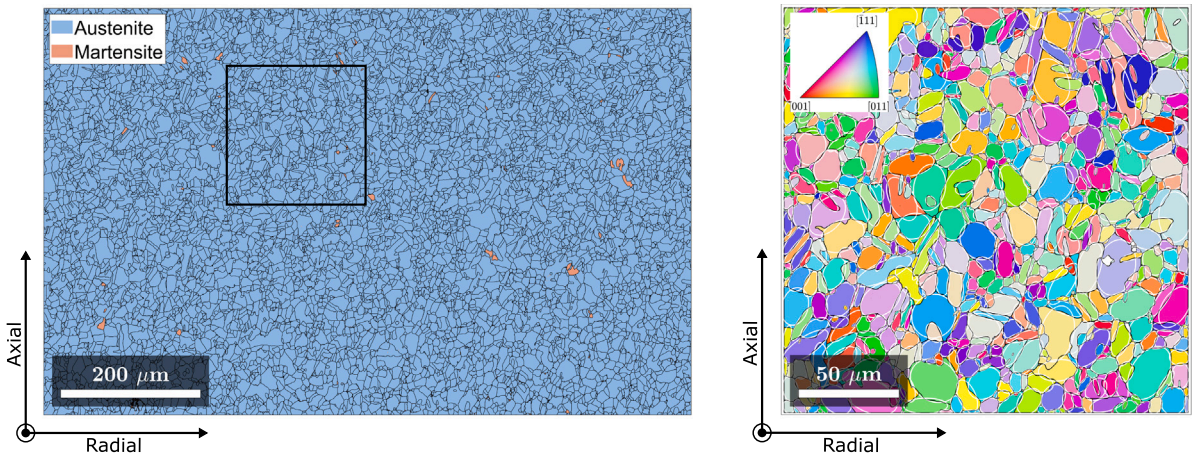


Fig. 1. Results of the EBSD measurement in terms of (a) phase distribution and (b) mean orientation as well as ellipses fitted to each grain within the region of interest (colored: Austenite, white: Martensite)

3.1. Microstructure reconstruction

As a mapper for the microstructure morphology, the aforementioned concept of SRVEs is employed. In this study, the SRVEs are generated with the RVE generator *DRAGen* [53]. *DRAGen* was developed within the author's group and is capable of mapping intricate microstructural characteristics, including grain shapes and sizes, martensite or pearlite banded structures, and martensitic or bainitic substructures [54]. A core feature of *DRAGen* is a deep-learning-based microstructure characterization algorithm, which learns the underlying joint distribution of microstructure descriptors like grain sizes or shapes and is afterwards capable of generating synthetic multivariate distributions of the microstructure descriptors [55]. For the reconstruction of the three-dimensional volume elements, *DRAGen* uses a cellular-automata-like approach consisting of first placing grains in a defined volume and subsequent growth of the grains until the volume is fully packed with material points. With this, complex microstructural morphology can be reconstructed accurately. In addition to the morphological properties of the grains, the crystallographic orientation of the grains is also reproduced in *DRAGen*. However, it should be noted that grain boundaries are not explicitly modeled in the approach used. Grain boundaries are only present in the SRVEs as differences in the crystallographic orientation. For detailed information on *DRAGen*, the reader is referred to Henrich et al. [53,54].

3.2. Crystal plasticity model

To model the mechanical behavior of the polycrystalline material, a crystal plasticity model is used. The concept of crystal plasticity itself is based on the pioneering work of Taylor from 1938 [56]. He first introduced the idea that deformation in crystals arises from slipping on specific slip planes and along slip directions, depending on the crystallographic orientation and the loading direction. However, it is assumed that all crystallites in a polycrystal undergo the same macroscopic deformation as the homogenized material, thus neglecting slip incompatibilities between individual grains. Therefore, a phenomenological crystal plasticity model is employed in this study, which is implemented in a UMAT subroutine for the commercial finite element solver Abaqus/Standard. The original formulation of phenomenological crystal plasticity, which dates back to the 1970s, was developed by Rice et al. [57], Hutchinson [58], and Peirce et al. [59,60]. The fundamental principle of this model family is the multiplicative decomposition of the deformation gradient $\mathbf{F}$ into an elastic and plastic part [61]:

$$\mathbf{F} = \mathbf{F}_\mathrm{e}\mathbf{F}_\mathrm{p} \tag{5}$$

$$\dot{\mathbf{F}}_\mathrm{p} = \mathbf{L}_\mathrm{p}\mathbf{F}_\mathrm{p} \tag{6}$$

$\mathbf{F}_\mathrm{e}$ and $\mathbf{F}_\mathrm{p}$ are the elastic and plastic components of the deformation gradient, respectively. The evolution of the plastic deformation gradient $\dot{\mathbf{F}}_\mathrm{p}$ is controlled by the plastic velocity gradient $\mathbf{L}_\mathrm{p}$, which is calculated as follows:

$$\mathbf{L}_\mathrm{p} = \sum_{\alpha=1}^{N_\mathrm{s}} \dot{\gamma}^\alpha \mathbf{m}^\alpha \otimes \mathbf{n}^\alpha \tag{7}$$

with N_s as the number of active slip systems. As austenite shows a face-centered cubic crystal structure, $N_\mathrm{s} = 12$ slip systems of type $\{111\}\langle 110\rangle$ are considered in this study. Further, $\dot{\gamma}^\alpha$ is the shear rate on a particular slip system α. $\mathbf{m}$ and $\mathbf{n}$ are the unit vectors for the normal of the slip plane and the slip direction, respectively. The shear rate $\dot{\gamma}^\alpha$ is computed based on the resolved shear stress τ^α following

$$\dot{\gamma}^\alpha = \dot{\gamma}_0 \left| \frac{\tau^\alpha - \chi^\alpha}{\tau_\mathrm{c}^\alpha} \right|^{\frac{1}{m}} \mathrm{sgn}(\tau^\alpha - \chi^\alpha) \tag{8}$$

Here, $\dot{\gamma}_0$ and m are material parameters, which have to be calibrated based on experimental data. χ^α is the backstress. The effect of the hardening on a particular slip system β on the hardening on another slip system α is expressed as:

$$\dot{\tau}_\mathrm{c}^\alpha = \sum_{\beta=1}^{N_\mathrm{s}} h_{\alpha\beta} \left| \dot{\gamma}^\beta \right| \tag{9}$$

The hardening matrix $h_{\alpha\beta}$ is defined as:

$$h_{\alpha\beta} = q_{\alpha\beta} \left[h_0 \left(1 - \frac{\tau_\mathrm{c}^\beta}{\tau_\mathrm{s}} \right)^a \right] \tag{10}$$

with h_0, τ_s and a as additional material parameters. The interaction matrix $q_{\alpha\beta}$ is a measure for the latent hardening with values of 1 for coplanar slip and 1.4 otherwise. Finally, the evolution of the backstress as a Frederick-Armstrong type model [62] is defined as:

$$\dot{\chi}^\alpha = A_1 \dot{\gamma}^\alpha - A_2 \chi^\alpha \left| \dot{\gamma}^\alpha \right| \tag{11}$$

A_1 and A_2 are additional material parameters, which have to be calibrated against hysteresis loops with a strain ration of $R_\varepsilon = -1$ to model the Bauschinger effect. The calibration of the model is conducted based on stable hysteresis loops, with the results shown in Section 4.3.

3.3. Fatigue indicator parameters

Within the context of microstructure-sensitive fatigue modeling, often so-called FIPs serve as a surrogate measure to describe local

phenomena of fatigue crack initiation, e.g., Dunne et al. [63] and Natkowski et al. [64]. Regarding the description of this fatigue damage phenomenon, there are a variety of different FIPs in the literature. In this study, two different FIP definitions are selected from literature, namely the accumulated plastic slip p and the strain energy density W as a strain- and energy-based criterion, respectively.

Manonukul and Dunne [38] introduced the accumulated plastic slip p as a definition of FIP. They assumed that the accumulation of small plastic strain increments is the main local driving force for fatigue crack initiation, as these strain increments can lead to the formation of persistent slip bands. When these persistent slip bands interfere with the lesser deformed matrix, the interfaces can act as potential sites for fatigue crack initiation. The validity of the usage of the accumulated plastic slip as a FIP was shown by Sharaf et al. [65] through a combination of experiments and crystal plasticity simulations. The formulation of the accumulated plastic slip reads as follows:

$$p = \int_0^t \sqrt{\frac{2}{3}\left(\mathbf{L}_\mathrm{p} : \mathbf{L}_\mathrm{p}\right)}\, \mathrm{d}t \tag{12}$$

As the accumulated plastic slip is solely incorporating local strain fields in its definition, local stress fields are neglected. However, Skelton [66] as well as Charkaluk and Constantinescu [67] assumed that the energy dissipation through dislocation motion serves as the driving force for fatigue crack initiation. Based on this assumption, Korsunsky et al. [68] defined the strain energy density to incorporate local stresses in the FIP definition, which can be read as:

$$W = \sum_{\alpha=1}^{N_\mathrm{s}} \int_0^t \tau^\alpha \dot{\gamma}^\alpha \, \mathrm{d}t \tag{13}$$

As the aforementioned FIPs are calculated in the integration point of each element, the FIP can be considered as a local measure of fatigue crack initiation. However, Boeff [69] showed that the FIP is highly depending on the discretization of the SRVE. Hence, a grain averaging scheme [70,71] was applied to convert the local FIP to a non-local FIP, resulting in a grain-averaged FIP for each grain. For further evaluations, only the maximum value from each simulation frame was taken as the non-local FIP. This approach can mathematically be described as follows:

$$FIP_\mathrm{M} = \max\left(\frac{1}{V_\mathrm{j}} \sum_{\mathrm{i}=1}^{N_\mathrm{j}} M_\mathrm{i,j} V_\mathrm{i,j}\right) \tag{14}$$

with $M \in \{p, W\}$ representing the accumulated plastic slip as well as the strain energy density of the ith element in the jth grain, respectively. Further, V_j describes the volume of the jth grain and N_j the number of elements as well as $V_\mathrm{i,j}$ the volume of the ith element in the jth grain.

3.4. Numerical lifetime prediction

In this study, an experimental short-time evaluation procedure is adapted for the first time in the framework of CPFEM to predict the finite fatigue life. The approach adapted here is called *MiDAcStrain* as introduced in previous work [16]. This novel lifetime prediction method allows the prediction of the finite fatigue life in the LCF regime solely based on a single strain increase test. The material's response M in terms of non-destructive testing-based measurements or the stress amplitude σ_a in the simplest case allows the calculation of incremental cyclic damage. By applying the damage rule according to Palmgren-Miner [13,14] virtual number of load cycles to failure can be calculated afterwards. As the material's response is depending on the local microstructure state and hence indicates the fatigue damage evolution during cyclic loading, a similarity is given with the meaning of FIPs. Hence, by adapting the *MiDAcStrain* approach, the aforementioned FIP definitions can be considered as the material's response in a numerical context.

In general, the number of cycles to failure N_i can be calculated by adapting the damage rule according to Palmgren-Miner [13,14] as

$$N_\mathrm{i} = \frac{n_\mathrm{i}}{d_\mathrm{i}} \tag{15}$$

Here, n_i represents the number of cycles according to Eq. (4) and d_i the incremental cyclic damage on the ith strain level, respectively. In the original *MiDAcStrain* approach [16], the incremental cyclic damage is calculated based on the experimentally determined strain energy density W following

$$d_\mathrm{i} = \frac{\int_{\varepsilon_\mathrm{a,t,i}-0.5\Delta\varepsilon_\mathrm{a,t}}^{\varepsilon_\mathrm{a,t,i}+0.5\Delta\varepsilon_\mathrm{a,t}} W}{\int_{\varepsilon_\mathrm{a,t,min}}^{\varepsilon_\mathrm{a,t,max}} W} \mathrm{d}\varepsilon \tag{16}$$

By substituting the experimentally determined strain energy density with the numerical material's response calculated in the form of the aforementioned FIPs, the incremental cyclic damage can be calculated as follows:

$$d_\mathrm{i} = \frac{\int_{\varepsilon_\mathrm{a,t,i}-0.5\Delta\varepsilon_\mathrm{a,t}}^{\varepsilon_\mathrm{a,t,i}+0.5\Delta\varepsilon_\mathrm{a,t}} FIP}{\int_{\varepsilon_\mathrm{a,t,min}}^{\varepsilon_\mathrm{a,t,max}} FIP} \mathrm{d}\varepsilon \tag{17}$$

Through discretization, this can further be simplified to

$$d_\mathrm{i} = \frac{FIP_\mathrm{i}}{\sum FIP_\mathrm{i}} \tag{18}$$

By combining Eqs. (15) and (18), the number of cycles to failure in the simulation $N_\mathrm{sim,i}$ can be calculated as

$$N_\mathrm{sim,i} = \frac{n_\mathrm{i} \cdot \sum FIP_\mathrm{i}}{FIP_\mathrm{i}} \tag{19}$$

Following the approach of Weber et al. [16] a correction factor f_cor is added, which reads as $f_\mathrm{cor} = 1/d_\mathrm{al}$. Here, d_al is the allowable damage sum, to correct the number of cycles to failure of the strain increase test to the ones of the individual constant amplitude tests due to load series effects [72], which was calculated in analogy to Palmgren-Miner [13,14] as follows:

$$d_\mathrm{al} = \sum_\mathrm{i} \frac{n_\mathrm{i}}{N_\mathrm{exp,i}} \tag{20}$$

Here, n_i are the number of cycles per strain level i according to Eq. (4) and $N_\mathrm{exp,i}$ are the respective experimentally determined number of cycles to failure, for example, through the *StrainLife* approach. Hence, the virtual number of cycles to failure can be calculated following

$$N_\mathrm{sim,i} = \frac{n_\mathrm{i}}{d_\mathrm{i}} \cdot \frac{1}{d_\mathrm{al}} \tag{21}$$

This allowable damage sum was determined in previous work [16] and ranges from $d_\mathrm{al} = 0.64$ to $d_\mathrm{al} = 0.84$, depending on the reference values used in the calculation. While $d_\mathrm{al} = 0.64$ results from using the fatigue lives determined by the *StrainLife* approach within Eq. (20), the value of $d_\mathrm{al} = 0.84$ results from using the fatigue lives, which were determined by fitting the Coffin-Manson-Basquin equation to the constant amplitude test data. As the *StrainLife* approach was already successfully validated in the literature [10,11,17,18], in this study we have chosen to apply the respective allowable damage sum of $d_\mathrm{al} = 0.64$, accordingly.

To apply the aforementioned lifetime prediction method, a strain increase test simulation was performed on all 20 generated SRVEs. The loading conditions in the simulations were identical to the experimental ones presented in Section 2.2. Periodic boundary conditions as well as the loading conditions presented in Fig. 2 were applied to each SRVE, where u denotes the displacement in the y-direction. The strain increase test simulations were initialized with a total strain amplitude of $\varepsilon_\mathrm{a,t,start} = 0.025\,\%$, increasing it step-wise after each 4 simulation cycles with an increment of $\Delta\varepsilon_{\mathrm{a,t_1}} = 0.025 \times 10^{-2}$. This increment was kept constant until a total strain amplitude of $\varepsilon_\mathrm{a,t} = 0.2\,\%$

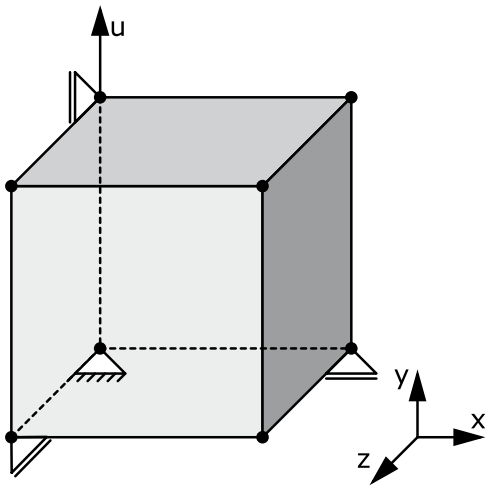


Fig. 2. Boundary and loading conditions of the SRVE.

was reached. Once this amplitude was reached, the increment was increased to $\Delta\varepsilon_{a,t_2} = 0.05 \times 10^{-2}$ until a total strain amplitude of $\varepsilon_{a,t} = 0.80\,\%$, where the specimen failed in the experiment. Hence, to ensure compatibility between experimental and virtual strain increase tests, the same strain levels and strain increments were applied to the simulations. This allowed to calculate the incremental cyclic damage on the same strain levels as in the experiment and hence allowed the application of the same allowable damage sum d_{al}. While the number of cycles spent on a strain level is decreased with increasing total strain amplitude in the experiment, in the simulations the load is always increased after just four cycles. As the FIP increment stabilizes after already a few cycles, ranging from two cycles [38] up to ten cycles [73], for computational efficiency, the cycle increment was kept low to an equal number of four cycles, so that the FIP could be extracted in the middle of each strain level following the experimental approach presented in previous work [16].

4. Results

The following sections present both the results of experimental fatigue tests as well as the simulation results after applying the newly adapted *MiDAcStrain*$_{CPFEM}$ approach. The latter includes the generation of several SRVEs as well as the parametrization of the crystal plasticity model. Numerically predicted fatigue lives are then compared to experimental data, which serves as the validation of the newly introduced numerical lifetime prediction method.

4.1. Experimental fatigue lives

Taking into account the experimental boundary conditions presented in Section 2.2 for the constant amplitude tests, Fig. 3(a) shows the respective evolution of stress amplitude for six selected total strain amplitudes over the whole range of applied load amplitudes. For the total strain amplitudes of $\varepsilon_{a,t} = 0.35\,\%$, $\varepsilon_{a,t} = 0.40\,\%$ and $\varepsilon_{a,t} = 0.50\,\%$, a slight increase in the stress amplitude caused by primary strain hardening can be observed at the beginning of the tests. After passing this primary hardening stage, a nearly constant stress amplitude level is first established. However, after this plateau, significant secondary hardening sets in, accompanied by an increase in the stress amplitude. This phenomenon can be correlated with the deformation-induced phase transformation of the austenitic phase into martensite as already shown in 1983 by Tsuzaki et al. [74]. When the accumulated plastic strain exceeds a critical threshold, the martensitic phase transformation sets in. Due to its diffusionless nature, a tetragonal distorted crystal lattice is formed, showing a significant increase in strength and hardness compared to the austenitic phase. Through its high dislocation density and complex internal stresses caused by the volumetric expansion, the newly formed martensite islands hinder dislocation slip, resulting in additional resistance to plastic deformation and hence macroscopic hardening. With an increasing number of applied cycles and hence further increasing accumulated plastic strain, the martensitic phase fraction also evolves steadily. After reaching a critical martensitic phase fraction, the former martensite islands coalesce to a martensitic network. As a result, the mechanical properties are increasingly determined by the martensitic phase. For the remaining total strain amplitudes of $\varepsilon_{a,t} = 0.80\,\%$, $\varepsilon_{a,t} = 1.00\,\%$ and $\varepsilon_{a,t} = 1.50\,\%$, a more pronounced hardening is present at the beginning of the tests, as the deformation-induced phase transformation already sets it during the primary strain hardening stage. Hence, a saturated stress level cannot be observed. While the evolution of the phase transformation during cyclic loading was not recorded, only post mortem measurements were performed in addition to the measurements performed directly before the tests, using a commercial FERITSCOPE® DMP® 30. All unloaded specimens showed 0 % of martensite volume fraction. Post mortem, a total of 10 measurements were performed per sample. The mean values as well as the respective standard deviations are listed in Table 2. While measuring the martensite volume fraction, a correction factor of 1.7 was applied to convert the FERITSCOPE® results to the actual martensite content as reported by Talonen et al. [75]. As the specimen loaded with $\varepsilon_{a,t} = 1.5\,\%$ showed distinct buckling, no measurement of the martensite volume fraction was performed. However, for the other amplitudes, it can be seen that with increasing total strain amplitude, the martensitic phase content after failure of the specimen also increases, showing a clear correlation. Since the objective of this study was to predict the fatigue life, the strain-life curve determined in a previous study [16] was employed. This curve, along with several constant amplitude tests (CATs) as well as the corresponding parameters of the Coffin-Manson-Basquin equation used to describe it, are given in Fig. 3(b) and Table 3, respectively. For additional details on the determination of these parameters, the reader is referred to Weber et al. [16].

Table 2
Post mortem measurements of the martensitic phase fraction on selected constant amplitude test specimens.

Total strain amplitude $\varepsilon_{a,t}$	Martensite volume fraction $f_{\alpha'}$
0.35 %	9.20 ± 1.83 %
0.40 %	31.88 ± 3.51 %
0.50 %	60.98 ± 2.64 %
0.80 %	74.98 ± 0.99 %
1.00 %	77.18 ± 5.53 %

Table 3
Parameters of the Coffin-Manson-Basquin equation determined by the *Strain-Life* approach adapted from previous work [16].

Parameter	Value	Unit
B	1.36	–
b	−0.16	–
C	12.51	–
c	−0.43	–

4.2. SRVE generation

Following the quantitative microstructure characterization step presented in Section 2.1, the collected distribution functions as well as their interdependencies serve as the input for the SRVE generation by *DRAGen* [53,54]. In total 20 cubic SRVEs were generated with an edge length of 50 µm, resulting in 179 ± 22 grains per SRVE. Each SRVE was meshed with 132 651 three-dimensional cubic elements with reduced integration (C3D8R) for the finite element solver ABAQUS/Standard.

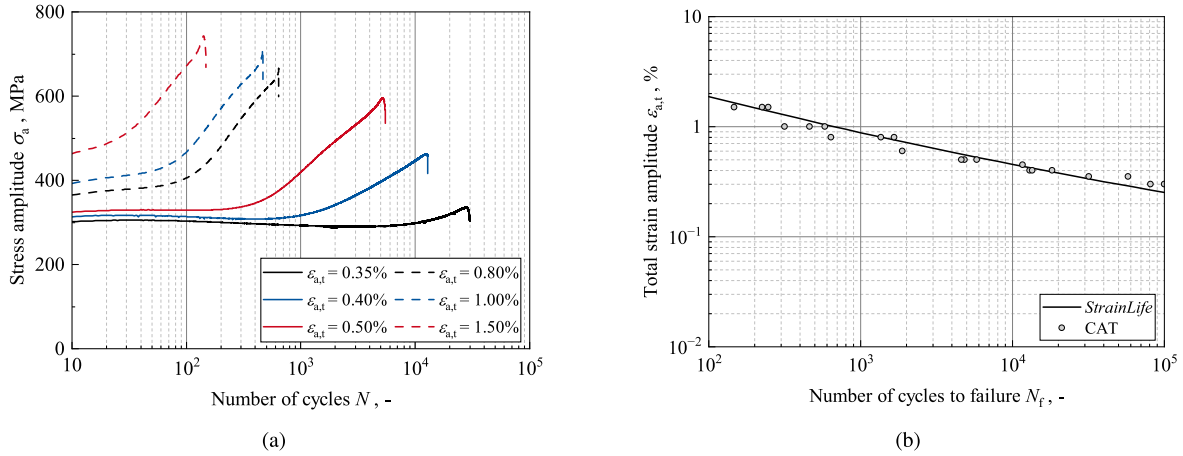


Fig. 3. Results of conducted fatigue tests: (a) evolution of stress amplitude for selected total strain amplitudes and (b) experimentally determined fatigue lives based on several constant amplitude tests (CATs) as well as the Coffin-Manson-Basquin fit according to the *StrainLife* approach.

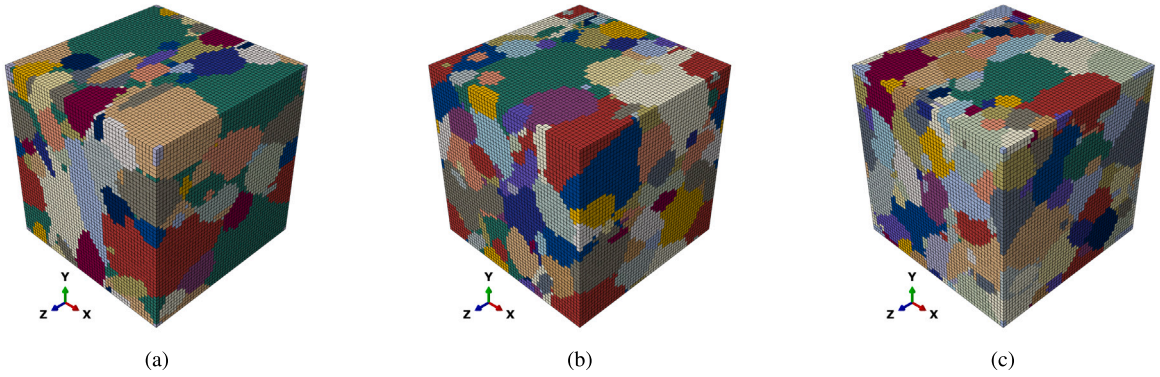


Fig. 4. Three examples out of 20 generated SRVEs for AISI 347 by *DRAGen* with (a) 142 grains, (b) 178 grains, and (c) 221 grains, representing the minimum, closest to the mean and maximum number of grains, respectively.

Fig. 4 shows three exemplary SRVEs. Even though every SRVE is unique and shows a different realization of the microstructure, they all follow the same underlying distribution functions, allowing the characterization of scatter within the simulation framework.

4.3. Parameter calibration

To correctly model the mechanical response in the SRVE simulations, the parameters of the crystal plasticity model presented in Section 3.2 were calibrated against experimental results. Often, the material parameters are calibrated against stable stress–strain hysteresis loops. However, as can be seen in Fig. 3(a), a nearly stable plateau is only present for the total strain amplitudes $\varepsilon_{a,t} = 0.35\,\%$, $\varepsilon_{a,t} = 0.40\,\%$ and $\varepsilon_{a,t} = 0.50\,\%$ up to approximately 10^4, 10^3 and 10^2 cycles, respectively. After this stable regime, secondary cyclic hardening sets in, which is caused by the deformation-induced martensitic phase transformation. Hence, the material parameters were calibrated and validated against the 100th load cycle for the aforementioned total strain amplitudes. Furthermore, as no isotropic hardening is present in this stable regime, only kinematic hardening is considered in the simulation, in accordance with Schäfer et al. [76]. Hence, by setting $h_0 = 0$ the isotropic hardening component was neglected. Therefore, only the elastic constants C_{11}, C_{12}, C_{44} as well as the parameters in the flow rule $\dot{\gamma}_0$, $\tau^{\alpha}_{c,0}$, m and both kinematic hardening parameters A_1 and A_2 had to be determined. The elastic constants were initially taken from Lee et al. [77] and multiplied with a factor of 0.75 to ensure the best fit to experimental data. The parameter $\dot{\gamma}_0 = 0.001$ was taken from literature [77–79] and $m = 0.05$ was chosen as the strain rate was kept constant throughout all simulations. Hence, only three parameters ($\tau^{\alpha}_{c,0}$, A_1 and A_2) had to be calibrated against experimental data. For the calibration process, the SRVE with 178 grains shown in Fig. 4(b) was used, as this represents the average number of grains in all SRVEs the closest. Depending on the total strain amplitude, the frequency in the simulation was adjusted to ensure the same constant strain rate as in the experimental investigations. The parameters were first were calibrated with a total strain amplitude of $\varepsilon_{a,t} = 0.40\,\%$ and afterwards validated against $\varepsilon_{a,t} = 0.35\,\%$ and $\varepsilon_{a,t} = 0.50\,\%$. The iterative calibration process was stopped once the simulation results matched the experimental results the closest. The comparison of simulation results after calibration with experimental stress–strain hysteresis loops of the 100th cycle are shown in Fig. 5. The simulation results agree well with the experimental data for all three investigated total strain amplitudes, and only slightly underestimate the plastic strain energy density, denoted as the area enclosed by the hysteresis loop. The errors are $-3.83\,\%$, $-4.78\,\%$ and $-8.67\,\%$ for $\varepsilon_{a,t} = 0.35\,\%$, $\varepsilon_{a,t} = 0.40\,\%$ and $\varepsilon_{a,t} = 0.50\,\%$, respectively. Hence, these parameters were used for all following simulations. All calibrated material parameters are listed in Table 4.

4.4. Lifetime prediction

Following the simulation setup and evaluation scheme presented in Section 3.4, the respective results are shown in the following figures. Fig. 6(a) and Fig. 6(b) present both the applied load in terms of the total strain amplitude as well as the numerical material's response in terms of both considered FIP definitions. While the applied total strain

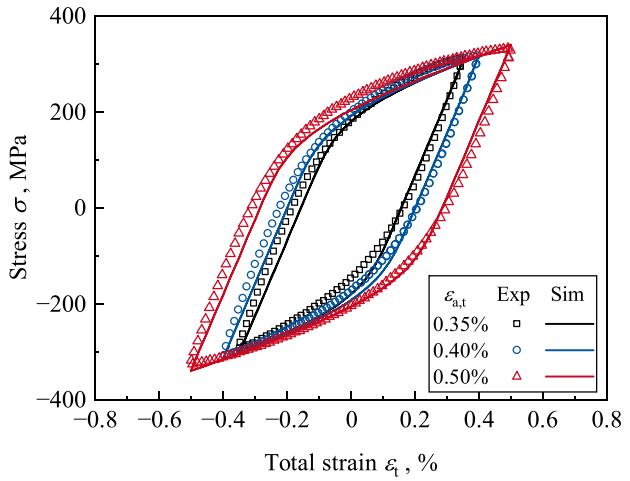


Fig. 5. Comparison of experimental stress–strain hysteresis loops with numerical results after crystal plasticity parameter calibration.

Table 4
Calibrated crystal plasticity parameters for AISI 347.

Parameter set	Parameter	Value	Unit
Elastic constants	C_{11}	181.50	GPa
	C_{12}	109.88	GPa
	C_{44}	84.00	GPa
Flow rule	$\dot{\gamma}_0$	0.001	s^{-1}
	$\tau^{\alpha}_{c,0}$	90	MPa
	m	0.05	–
Kinematic hardening	A_1	15 000	MPa
	A_2	25	–

amplitude follows a stepwise increase following a strain increase test, up to a total strain amplitude of $\varepsilon_{a,t} = 0.15\,\%$, both FIPs do not show a significant evolution and almost no deviation from the zero baseline. After further increasing the load, both FIPs start to show an exponential trend, reaching a maximum value at the end of the simulation of approximately 1.1 and 214 MJ m^{-3} for FIP_p and FIP_W, respectively. Additionally, the standard deviations represented as error bars in both figures also increase with increasing applied total strain amplitude, reaching maximum absolute values of approximately ±0.09 and ±20 MJ m^{-3}, and relative values of approximately 8.18 % and 9.35 %.

By constructing a Morrow diagram [80] by plotting both FIPs as the material's response as a function of the applied total strain amplitude, as shown in Fig. 6(c) and Fig. 6(d), a similar trend as described earlier is maintained, showing exponential growth for both FIPs. By applying Eq. (18), the incremental cyclic damage can be calculated from both FIP formulations. When plotting the respective incremental cyclic damage against the applied load amplitude, Fig. 6(e) and Fig. 6(f) are obtained for FIP_p and FIP_W. Both curves again follow an exponential trend starting at around a total strain amplitude of $\varepsilon_{a,t} = 0.15\,\%$. As can be seen, both curves reach similar values for all applied loads. For example, for a total strain amplitude of $\varepsilon_{a,t} = 0.40\,\%$, FIP_p reaches an incremental cyclic damage value of approximately 0.04, while FIP_W reaches a value of approximately 0.03. For a total strain amplitude of $\varepsilon_{a,t} = 0.80\,\%$, FIP_p reaches an incremental cyclic damage of approximately 0.18, while FIP_W reaches a value of approximately 0.20. Contrary to the FIP evolutions shown previously, the standard deviations of the incremental cyclic damage are much smaller, reaching a maximum of approximately 2.07 % and 1.12 % for FIP_p and FIP_W, respectively.

Based on this calculated incremental cyclic damage, virtual lifetimes were calculated by applying Eq. (21) with $d_{al} = 0.64$, which was determined through Eq. (20) in previous work [16]. In addition, an allowable damage sum of $d_{al} = 1.00$ is considered, mimicking the case where no value for the allowable damage sum is available. As presented in Section 3.4, all simulations were performed up to a total strain amplitude of $\varepsilon_{a,t} = 0.8\,\%$, which is consistent with the experimental strain level at fracture in the strain increase test [16]. Hence, only FIP values as well as incremental cyclic damage values up to $\varepsilon_{a,t} = 0.8\,\%$ can be extracted and calculated from the simulations. Therefore, predictions of virtual lifetimes are only possible up to this particular strain level. This further allowed to apply the allowable damage sum d_{al} determined from the experiments. The virtual data pairs of the strain-life curve for both d_{al} values are shown in Fig. 7(a) and Fig. 7(b) for FIP_p and FIP_W. Additionally, experimental constant amplitude tests as well as the strain-life curve determined in previous work [16] are also shown. The latter is decomposed into its elastic and plastic components, which can be described by Basquin's law [46] and the Coffin-Manson relation [44,45]. As can be seen, the simulation-based lifetimes, considering $d_{al} = 0.64$, for both FIPs agree very well with the experimental results, especially with the fitted total strain curve from *StrainLife*. The effect by setting $d_{al} = 1.00$ is also clearly visible. By increasing d_{al}, the lifetimes are shifted to lower values, hence delivering more conservative results. Due to the small standard deviations already present in the calculation of the incremental cyclic damage, the virtual lifetimes also show only small scatter.

5. Discussion

The adaptation of experimentally validated short-time evaluation procedures to the framework of microstructure-sensitive fatigue modeling was shown to be a feasible measure to accelerate fatigue life prediction while maintaining high predictive accuracy. However, several aspects have to be addressed and discussed. The following sections hence first critically address the adapted lifetime prediction method and its underlying lifetime calculation scheme. Finally, the constitutive model used to predict the polycrystalline material behavior is discussed with an emphasis on additional micromechanical phenomena neglected in this study.

5.1. Lifetime prediction

When comparing the numerically predicted fatigue lives for $d_{al} = 0.64$ with the experimentally determined fatigue lives as shown in Fig. 7(a) and Fig. 7(b), at first glance, a very good agreement can be observed. However, a more detailed comparison can be conducted when plotting the virtual lifetimes against the experimental lifetimes determined through *StrainLife*. From Fig. 8(a), it becomes apparent that between approximately 1500 and 17 000 load cycles, the virtual lifetimes based on FIP_p deviate from the diagonal, representing a perfect match. However, all of them fall within the ±1.5 scatter band, still showing reasonable agreement. For higher cycle counts of up to 100 000, the simulation results almost coincide perfectly with the experimental values. Contrary to the FIP_p-based results, the virtual lifetimes based on the FIP_W calculations, as shown in Fig. 8(b), slightly overestimate the number of cycles to failure over the whole LCF regime limited by 100 000 cycles. Nevertheless, all of them lie within the ±1.5 scatter band, still showing good agreement with experimental data. By applying an allowable damage sum of $d_{al} = 1.00$, which is equivalent to neglecting the existence of an allowable damage sum, the virtual lifetimes are shifted to lower values, resulting in a more conservative estimate. For both FIP definitions, the adjusted lifetimes still mainly lie within the ±1.5 scatter band. Hence, even when there is no prior knowledge of the applicable allowable damage sum, assuming $d_{al} = 1.00$ yields a more conservative but still reasonable estimate of the fatigue life. As the scatter from these 20 SRVE simulations is also very small, it can be concluded that only a single SRVE simulation is enough to predict whole ε-N curves with reasonable accuracy.

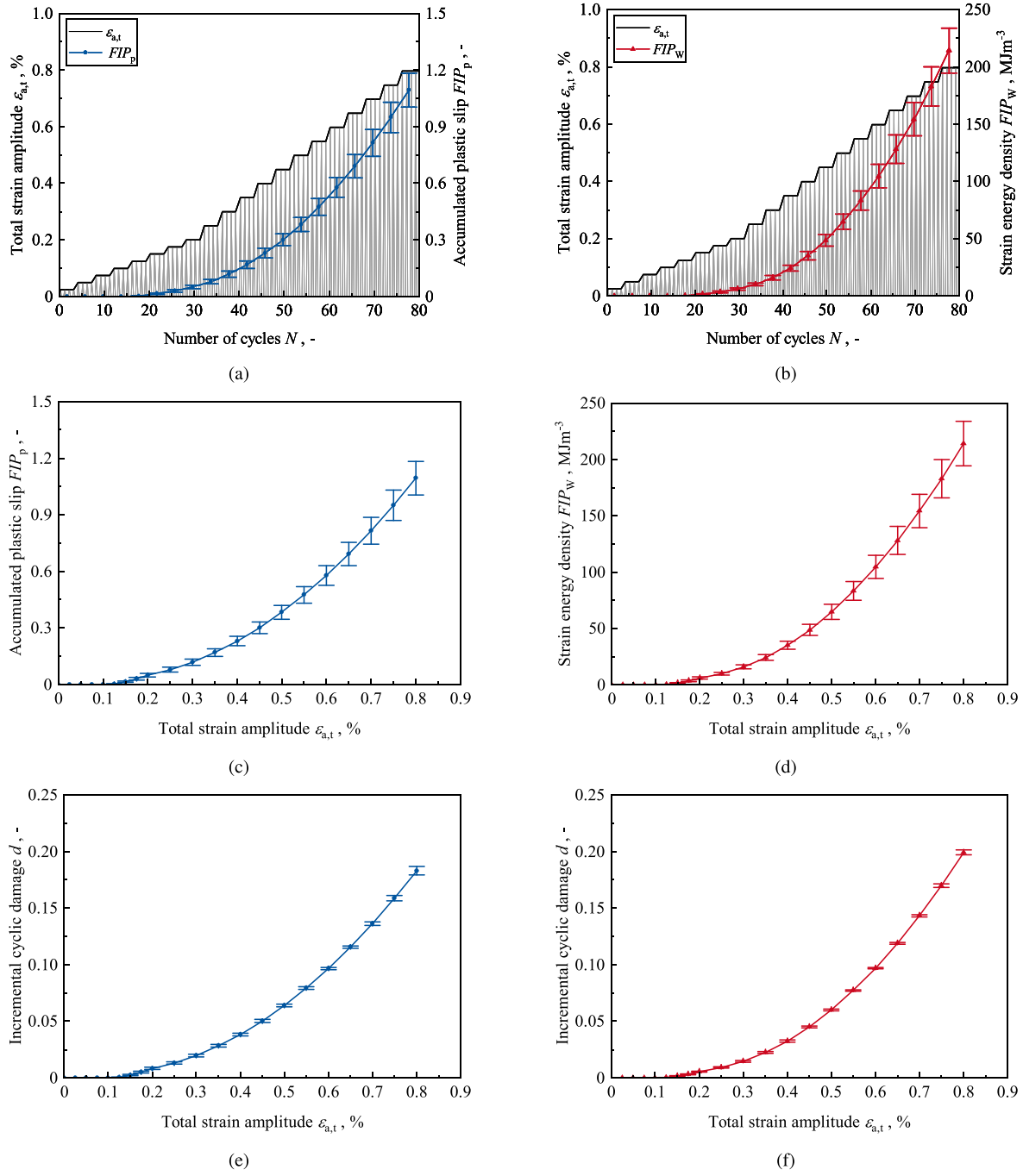


Fig. 6. Evaluation scheme according to the *MiDAcStrain*$_{CPFEM}$ approach: (a)(b) numerical results of the strain increase test simulations with FIP_p and FIP_W as the material's response, (c)(d) both FIP results as a function of the total strain amplitude and (e)(f) calculated incremental cyclic damage from both FIPs.

While in this study, FIPs based on the accumulated plastic slip p and the strain energy density W were considered, several other FIP definitions exist in the literature. For example, related to the work of Fatemi and Socie [81] and their FIP based on the critical plane approach, Castelluccio and McDowell [82] introduced a crystallographic version of said FIP to quantify driving forces for transgranular failure in micromechanical simulations. By adapting this FIP formulation, the fatigue life can be captured with good accuracy [64,83]. Based on the strain energy density FIP introduced by Korsunsky et al. [68], Zinovev [84] incorporated the backstress into the FIP definition to model grain boundary cracking in thermomechanical fatigue of ITER relevant tungsten. While the adapted FIPs in this article successfully serve as a numerical surrogate of the material's response to predict virtual fatigue lives, other FIP definitions should also be investigated with respect to their applicability within the newly introduced lifetime prediction method.

Additionally, the determination and role of the allowable damage sum d_{al} introduced in Eq. (21) have to be addressed critically. While the previously presented results are only valid for an allowable damage sum of $d_{al} = 0.64$, by changing this parameter, the virtual lifetimes can be shifted horizontally, resulting in lower or higher predicted fatigue lives. Hence, the determination of this value is of particular importance. Even though this parameter could in general be treated as a fitting parameter similar to FIP_{crit} and p in Eq. (1) or $FIP_{irr,crit}$ in Eq. (2), in this study the allowable damage sum determined experimentally in previous work [16] was adapted, resulting in closely matching

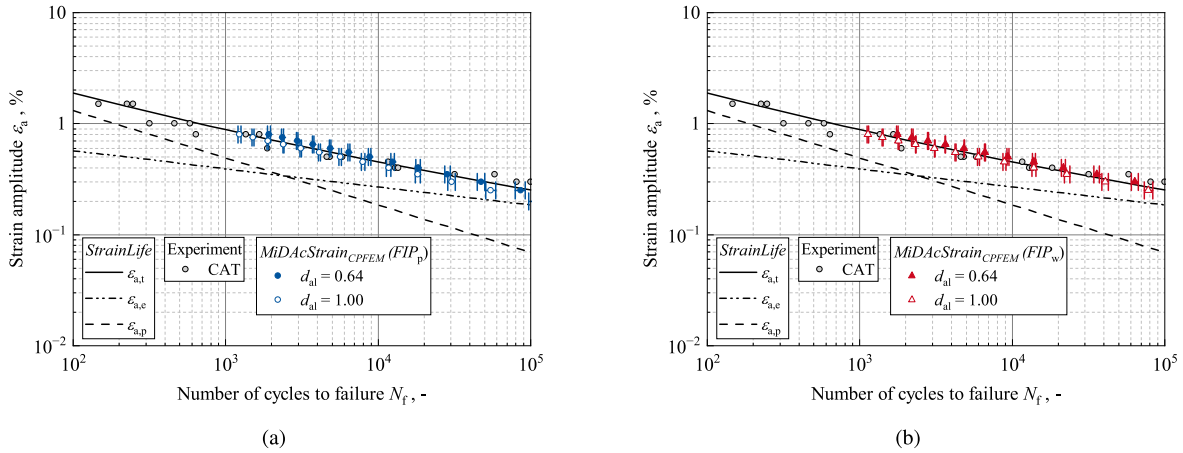


Fig. 7. Comparison of numerically predicted fatigue lives with experimental results, i.e., *StrainLife* curves and constant amplitude tests (CATs), based on (a) FIP_p and (b) FIP_w.

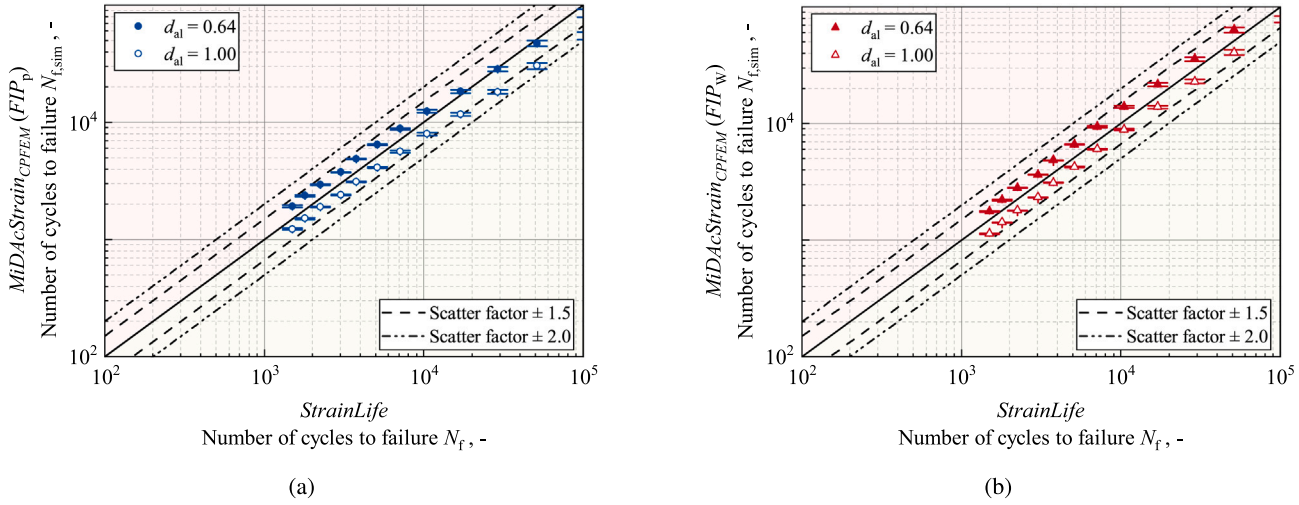


Fig. 8. Validation of the numerically predicted fatigue lives with experimental data for (a) FIP_p and (b) FIP_w.

fatigue lives. Hence, by considering this allowable damage sum as a material constant, which can be applied both in experimental and numerical accelerated lifetime prediction methods, fast and reliable fatigue life predictions can be made without the need to determine additional fitting parameters. However, future work should address the determination of this allowable damage sum in more detail and check the validity of this assumption for other steel grades or materials in general.

5.2. Martensitic phase transformation

As was described in Section 4.1, a deformation-induced phase transformation from austenite to martensite takes place, which is accompanied by a significant change in the mechanical properties of the material under investigation. The role of this phase transformation on the cyclic properties – in particular, the initiation and growth of fatigue cracks and, consequently, the fatigue life – has been a focus of research for many decades. Already in 1983, Tsuzaki et al. [74] summarized the overall effect of the phase transformation on finite fatigue life in general as follows: At high loading amplitudes, when the martensite forms before the fatigue crack is initiated, due to its brittleness and poor fracture toughness, the fresh martensite islands act as preferential sites for fatigue crack initiation. Additionally, the cyclic tensile stress increases during loading, which further promotes fatigue crack propagation, finally decreasing the fatigue life. However, at low loading conditions, if martensite is formed around the crack tip after the fatigue crack is initiated, not only the strain energy absorbed at the crack tip [85], which otherwise would promote fatigue crack growth, but also compressive stresses due to the volumetric expansion of the crystal lattice [86] suppress fatigue crack propagation, effectively prolonging the fatigue life. In a recent study by Wang et al. [87] this dual role of martensitic phase transformation with regard to fatigue crack growth was investigated for a medium-Mn TRIP steel. In this study, the authors not only summarized different mechanisms postulated in the literature over time, but further revealed two additional fatigue mechanisms. It can therefore be concluded that, to this day, the effects of deformation-induced phase transformation on the cyclic properties – and, consequently, on fatigue life – are not fully understood or generally accepted. Hence, the need to accurately describe and develop respective material models explicitly considering this martensitic phase transformation is given. While several material models already exist to explicitly consider this deformation-induced phase transformation on the micro-scale for quasi-static loading, e.g., by Ma and Hartmaier [78] or Gupta et al. [88], who extended this model to include also short- and long-range interactions through geometrically necessary dislocations, only limited literature is available where such kind of model is used to predict fatigue lives. Recently, Moore et al. [89] predicted the fatigue life of NiTi, modeling the reversible martensitic phase transformation

and evaluating the influence of the martensitic volume fraction on FIPs. However, in metastable austenitic stainless steels, this phase transformation is irreversible and evolves non-linearly over the whole lifespan in a constant amplitude test. Hence, it would be necessary to explicitly model the whole lifetime, e.g., 100 000 load cycles in the LCF regime, which is, however, computationally not feasible. Hence, in this study, a simplified regular crystal plasticity model was adapted, not taking into account the deformation-induced phase transformation and its influence on the mechanical properties. Nonetheless, even by neglecting the deformation-induced phase transformation in the adapted numerical lifetime prediction method presented in this study, high predictive accuracy is achieved, while focusing solely on predicting macroscopic fatigue lives. Future work, however, should focus on developing models that explicitly incorporate the deformation-induced phase transformation into the constitutive laws for cyclic loading scenarios. By doing so, even more accurate fatigue life estimates should be generated.

6. Conclusion

The present article introduces a new approach to accelerate numerical fatigue life predictions in the LCF regime by adapting experimentally validated short-time evaluation procedures to the framework of microstructure-sensitive fatigue modeling. By performing strain increase test simulations on multiple SRVEs, it was shown that fatigue indicator parameters can be used as a numerical surrogate of the material's response, which serves as the foundation to calculate incremental cyclic damage. From this incremental damage, virtual lifetimes can then be calculated for each load level covered in the simulation. While the predicted fatigue lives are depending on the allowable damage sum d_{al}, which could be treated in general as a fitting parameter, it was shown, that the experimentally determined value of d_{al} can also be applied in numerical simulations, delivering good accuracy. Experimental and virtual lifetimes coincide reasonably well and fall within a $\pm$ 1.5 scatter band. Both FIPs used in this study, namely the accumulated plastic slip p and the strain energy density W deliver similar results, while slightly overestimating the number of cycles to failure. By performing a strain increase test simulation, the lifetime for several amplitudes can be computed at once, eliminating the necessity to conduct multiple SRVE simulations over a wide range of load levels, hence accelerating numerical fatigue life predictions. However, due to the small scatter in the virtual fatigue lives, only trend curves can be determined. A probabilistic analysis and the calculation of failure or survival probabilities are not possible, which limits its application in the practical design of components. Nevertheless, the method presented in this study can still be used for a quick initial estimate of fatigue life, yielding reasonable results. Nonetheless, future work should address the validity of the allowable damage sum to be used as a material constant in both experimental and numerical accelerated lifetime prediction methods. Additionally, the effect of the deformation-induced martensitic phase transformation should be considered in the formulation of the constitutive laws, which was neglected in this study. While the present study focused on the LCF regime, an adaptation for the HCF regime also seems possible.

CRediT authorship contribution statement

Christian Häffner: Writing – original draft, Visualization, Methodology, Investigation, Formal analysis, Data curation, Conceptualization. **Niklas C. Fehlemann:** Writing – original draft. **Sophie C. Stebner:** Writing – review & editing, Project administration. **Felix Weber:** Writing – review & editing. **Sebastian Münstermann:** Writing – review & editing, Supervision.

Declaration of competing interest

The authors declare that they have no known competing financial interests or personal relationships that could have appeared to influence the work reported in this paper.

Acknowledgments

This research was supported by the Federal Ministry for the Environment, Climate Action, Nature Conservation and Nuclear Safety based on a decision of the German Bundestag (grant number 1501656). Computations were performed with computing resources granted by RWTH Aachen University under project rwth1684.

Data availability

The data that support the findings of this study are available from the corresponding author upon reasonable request.

References

[1] DIN Deutsches Institut für Normung eV. DIN EN 6072 Aerospace series – Metallic materials – Test methods – Constant amplitude fatigue testing. 2011.
[2] International Organization for Standardization. ISO/DIS 12106 Metallic materials – Fatigue testing – Axial-strain-controlled method. 2025.
[3] ASTM International. E606/E606M – Standard test method for strain-controlled fatigue testing. 2021.
[4] Koller R, Ruiz-Ripoll ML, García A, Fernández-Canteli A, Castillo E. Experimental validation of a statistical model for the Wöhler field corresponding to any stress level and amplitude. Int J Fatigue 2009;31(2):231–41. http://dx.doi.org/10.1016/j.ijfatigue.2008.09.003.
[5] Scholl LM, Tegeder F, Hajeck T, Bezold A, Broeckmann C. Toward the application of multiaxial failure criteria: mean stress sensitivity of carbide–rich, high–alloy PM–HIP tool steels under axial and torsional cyclic loading. Steel Res Int 2026. http://dx.doi.org/10.1002/srin.202501036.
[6] Stopka KS, Sangid MD. A unified model for microstructure-sensitive fatigue crack initiation across low and high cycle fatigue. Mater Des 2026;261:115382. http://dx.doi.org/10.1016/j.matdes.2025.115382.
[7] Starke P, Walther F, Eifler D. "PHYBAL" a short–time procedure for a reliable fatigue life calculation. Adv Eng Mater 2010;12(4):276–82. http://dx.doi.org/10.1002/adem.200900344.
[8] Starke P. StressLife$_{fc}$ – NDT-related assessment of the fatigue life of metallic materials. Mater Test 2019;61(4):297–303. http://dx.doi.org/10.3139/120.111319.
[9] Weber F, Koziol J, Starke P. StressLife: A short-time approach for the teter-mination of a trend S-N curve in and beyond the HCF regime for the steels 20MnMoNi5-5 and SAE 1045. Materials 2023;16(11). http://dx.doi.org/10.3390/ma16113914.
[10] Acosta R, Boller C, Starke P, Jamrozy M, Knyazeva M, Walther F, Heckmann K, Sievers J, Schopf T, Weihe S. Non-destructive testing derived parameters for microstructure-based residual service life assessment of aging metallic materials in nuclear engineering. Mater Test 2019;61(11):1029–38. http://dx.doi.org/10.3139/120.111417.
[11] Acosta R, Heckmann K, Sievers J, Schopf T, Bill T, Starke P, Donnerbauer K, Lücker L, Walther F, Boller C. Microstructure-based lifetime assessment of austenitic steel AISI 347 in view of fatigue, environmental conditions and NDT. Appl Sci 2021;11(23):11214. http://dx.doi.org/10.3390/app112311214.
[12] Weber F, Wu H, Starke P. A new short-time procedure for fatigue life evaluation based on the linear damage accumulation by Palmgren–Miner. Int J Fatigue 2023;172:107653. http://dx.doi.org/10.1016/j.ijfatigue.2023.107653.
[13] Palmgren A. The service life of ball bearings. Z Vereins Dtsch Ingen 1924;68(14):339–41.
[14] Miner MA. Cumulative damage in fatigue. J Appl Mech 1945;12(3):A159–64. http://dx.doi.org/10.1115/1.4009458.
[15] Weber F, Weber F, Sedlatschek T, Bezold A, Broeckmann C, Starke P. Microstructure-specific lifetime prediction method for heavy-section castings based on non-destructive measurements during fatigue testing. Int J Met 2025. http://dx.doi.org/10.1007/s40962-025-01816-z.
[16] Weber F, Häffner C, Weber F, Stebner SC, Broeckmann C, Müntermann S. MiDAcStrain – a novel lifetime prediction method in the low cycle fatigue regime. 2026, http://dx.doi.org/10.2139/ssrn.7269919, Preprint at SSRN.
[17] Bill T, Acosta R, Boller C, Donnerbauer K, Lücker L, Walther F, Heckmann K, Sievers J, Schopf T, Weihe S, Starke P. A short-time approach for fatigue life evaluation of AISI 347 steel for nuclear power energy applications. Appl Sci 2021;11(23):11405. http://dx.doi.org/10.3390/app112311405.
[18] Donnerbauer K, Bill T, Starke P, Acosta R, Yerrapa B, Boller C, Heckmann K, Sievers J, Walther F. Fatigue life evaluation of metastable austenitic stainless steel AISI 347 based on nondestructive testing methods for different environmental conditions. Int J Fatigue 2024;179:108056. http://dx.doi.org/10.1016/j.ijfatigue.2023.108056.

[19] Koch A, Mrzljak S, Strodick S, Walther F. Sustainable fatigue characterization of metals: Hysteresis-life – a universal short-time test method for resource-efficient fatigue life assessment. Procedia CIRP 2026;140:910–5. http://dx.doi.org/10.1016/j.procir.2026.05.153.

[20] Gu Y, Zhang C, Zhang P, Golub MV, Yu B. Enriched physics-informed neural networks for 2D in-plane crack analysis: Theory and MATLAB code. Int J Solids Struct 2023;276:112321. http://dx.doi.org/10.1016/j.ijsolstr.2023.112321.

[21] Zhang P, Gu Y, Xie L, Altay O, Zhang C, Babeshko V. A novel boundary-based machine learning approach for 2D crack analysis in elastic and piezoelectric materials. Comput Methods Appl Mech Engrg 2026;449:118531. http://dx.doi.org/10.1016/j.cma.2025.118531.

[22] Chen Z, Dai Y, Liu Y. Crack propagation simulation and overload fatigue life prediction via enhanced physics-informed neural networks. Int J Fatigue 2024;186:108382. http://dx.doi.org/10.1016/j.ijfatigue.2024.108382.

[23] Zhou S, Häffner C, Wang S, Stebner S, Liao Z, Yang B, Wei Z, Münstermann S. Transfer-learned Kolosov–Muskhelishvili informed neural networks for fracture mechanics. Theor Appl Fract Mech 2026;144:105582. http://dx.doi.org/10.1016/j.tafmec.2026.105582.

[24] Hu Z, Ruan X, Sun H, Wang G, Liao Z, Chen H. Optimized neural network and finite element method for accurate fatigue crack growth path prediction. Int J Fatigue 2026;209:109651. http://dx.doi.org/10.1016/j.ijfatigue.2026.109651.

[25] Liu Y-K, Fan J-L, Zhu G, Zhu M-L, Xuan F-Z. Data-driven approach to very high cycle fatigue life prediction. Eng Fract Mech 2023;292:109630. http://dx.doi.org/10.1016/j.engfracmech.2023.109630.

[26] Liang Z, Wang X, Cui Y, Xu W, Zhang Y, He Y. A new data-driven probabilistic fatigue life prediction framework informed by experiments and multiscale simulation. Int J Fatigue 2023;174:107731. http://dx.doi.org/10.1016/j.ijfatigue.2023.107731.

[27] Feng F, Zhu T, Yang B, Zhou S, Xiao S. A physics-informed neural network approach for predicting fatigue life of SLM 316L stainless steel based on defect features. Int J Fatigue 2024;188:108486. http://dx.doi.org/10.1016/j.ijfatigue.2024.108486.

[28] Tang C-Z, Li H-W, Li K-S, Lei X-L, Cheng L-Y, Ju L, Li W, Zeng F, Zhang X-C. Data-driven fatigue life prediction of small-deep holes in a nickel-based superalloy after a cold expansion process. Int J Fatigue 2024;181:108159. http://dx.doi.org/10.1016/j.ijfatigue.2024.108159.

[29] Wang H, Li B, Gong J, Xuan F-Z. Machine learning-based fatigue life prediction of metal materials: Perspectives of physics-informed and data-driven hybrid methods. Eng Fract Mech 2023;284:109242. http://dx.doi.org/10.1016/j.engfracmech.2023.109242.

[30] McDowell DL, Dunne F. Microstructure-sensitive computational modeling of fatigue crack formation. Int J Fatigue 2010;32(9):1521–42. http://dx.doi.org/10.1016/j.ijfatigue.2010.01.003.

[31] Lebensohn RA. N-site modeling of a 3D viscoplastic polycrystal using fast fourier transform. Acta Mater 2001;49(14):2723–37. http://dx.doi.org/10.1016/S1359-6454(01)00172-0.

[32] Roters F, Diehl M, Shanthraj P, Eisenlohr P, Reuber C, Wong SL, Maiti T, Ebrahimi A, Hochrainer T, Fabritius H-O, Nikolov S, Friák M, Fujita N, Grilli N, Janssens K, Jia N, Kok P, Ma D, Meier F, Werner E, Stricker M, Weygand D, Raabe D. DAMASK – the düsseldorf advanced material simulation kit for modeling multi-physics crystal plasticity, thermal, and damage phenomena from the single crystal up to the component scale. Comput Mater Sci 2019;158:420–78. http://dx.doi.org/10.1016/j.commatsci.2018.04.030.

[33] Lebensohn RA, Rollett AD. Spectral methods for full-field micromechanical modelling of polycrystalline materials. Comput Mater Sci 2020;173:109336. http://dx.doi.org/10.1016/j.commatsci.2019.109336.

[34] Loiodice L, Stopka KS, Sangid MD. A workflow to accelerate microstructure–sensitive fatigue life predictions. Adv Eng Mater 2025. http://dx.doi.org/10.1002/adem.202502138.

[35] Liu P, Chen Z, Xu C, Dong J, Jiang H. A crystal plasticity phase-field model for microstructure sensitive fatigue crack growth in a superalloy. Eng Fract Mech 2024;311:110526. http://dx.doi.org/10.1016/j.engfracmech.2024.110526.

[36] Lucarini S, Dunne F, Martínez-Pañeda E. An FFT-based crystal plasticity phase-field model for micromechanical fatigue cracking based on the stored energy density. Int J Fatigue 2023;172:107670. http://dx.doi.org/10.1016/j.ijfatigue.2023.107670.

[37] Cruzado A, Lucarini S, LLorca J, Segurado J. Microstructure-based fatigue life model of metallic alloys with bilinear Coffin-Manson behavior. Int J Fatigue 2018;107:40–8. http://dx.doi.org/10.1016/j.ijfatigue.2017.10.014.

[38] Manonukul A, Dunne FPE. High- and low-cycle fatigue crack initiation using polycrystal plasticity. Proc R Soc Lond A 2004;460(2047):1881–903. http://dx.doi.org/10.1098/rspa.2003.1258.

[39] Boeff M, Hassan Hu, Hartmaier A. Micromechanical modeling of fatigue crack initiation in polycrystals. J Mater Res 2017;32(23):4375–86. http://dx.doi.org/10.1557/jmr.2017.384.

[40] Mughrabi H. Cyclic slip irreversibilities and the evolution of fatigue damage. Metall Mater Trans B 2009;40(4):431–53. http://dx.doi.org/10.1007/s11663-009-9240-4.

[41] Mughrabi H. Cyclic slip irreversibility and fatigue life: A microstructure-based analysis. Acta Mater 2013;61(4):1197–203. http://dx.doi.org/10.1016/j.actamat.2012.10.029.

[42] Sayer N, Natkowski E, Sonnweber-Ribic P, Münstermann S. A novel microscale fatigue failure indicator considering plastic irreversibility for microstructure-based lifetime simulation. Int J Fatigue 2022;163:107115. http://dx.doi.org/10.1016/j.ijfatigue.2022.107115.

[43] He J, Hu C, Zhang R, Hu P, Xiao C, Wang X. A new low-cycle and high-cycle fatigue life prediction criterion based on crystal plasticity finite element method. Int J Fatigue 2025;197:108903. http://dx.doi.org/10.1016/j.ijfatigue.2025.108903.

[44] Coffin LF. A study of the effects of cyclic thermal stresses on a ductile metal. J Fluids Eng 1954;76(6):931–49. http://dx.doi.org/10.1115/1.4015020.

[45] Manson SS. Technical note 2933: Behavior of materials under conditions of thermal stress. 1953,

[46] Basquin OH. The exponential law of endurance tests. Proc Am Soc Test Mater 1910;10:625–30.

[47] DIN Deutsches Institut für Normung eV. DIN EN 10027-1 Designation systems for steels – Part 1: Steel names. 2017.

[48] DIN Deutsches Institut für Normung eV. DIN EN 10027-2 Designation systems for steels – Part 2: Numerical system. 2015.

[49] Nuclear Safety Standards Commission. KTA 3201.1 Components of the reactor coolant pressure boundary of light water reactors – Part 1: materials and product forms. 2017, URL https://www.kta-gs.de/e/standards/3200/3201_1_engl_2017_11_ber.pdf.

[50] Bachmann F, Hielscher R, Schaeben H. Texture analysis with MTEX – Free and open source software toolbox. Solid State Phenom 2010;160:63–8. http://dx.doi.org/10.4028/www.scientific.net/SSP.160.63.

[51] Bachmann F, Hielscher R, Schaeben H. Grain detection from 2d and 3d EBSD data – Specification of the MTEX algorithm. Ultramicroscopy 2011;111(12):1720–33. http://dx.doi.org/10.1016/j.ultramic.2011.08.002.

[52] Mulchrone KF, Choudhury KR. Fitting an ellipse to an arbitrary shape: Implications for strain analysis. J Struct Geol 2004;26(1):143–53. http://dx.doi.org/10.1016/S0191-8141(03)00093-2.

[53] Henrich M, Pütz F, Münstermann S. A novel approach to discrete representative volume element automation and generation-DRAGen. Materials 2020;13(8). http://dx.doi.org/10.3390/ma13081887.

[54] Henrich M, Fehlemann N, Bexter F, Neite M, Kong L, Shen F, Könemann M, Dölz M, Münstermann S. DRAGen - a deep learning supported RVE generator framework for complex microstructure models. Heliyon 2023;9(8):e19003. http://dx.doi.org/10.1016/j.heliyon.2023.e19003.

[55] Fehlemann N, Sparrer Y, Pütz F, Konemann M, Münstermann S. Influence of synthetically generated inclusions on the stress accumulation and concentration in X65 pipeline steel. IOP Conf Ser: Mater Sci Eng 2021;1157(1):012056. http://dx.doi.org/10.1088/1757-899X/1157/1/012056.

[56] Taylor GI. Plastic strain in metals. J Inst Met 1938;62:307–24.

[57] Rice JR. Inelastic constitutive relations for solids: An internal-variable theory and its application to metal plasticity. J Mech Phys Solids 1971;19(6):433–55. http://dx.doi.org/10.1016/0022-5096(71)90010-X.

[58] Hutchinson JW. Bounds and self-consistent estimates for creep of polycrystalline materials. Proc R Soc Lond A 1976;348(1652):101–27. http://dx.doi.org/10.1098/rspa.1976.0027.

[59] Peirce D, Asaro RJ, Needleman A. An analysis of nonuniform and localized deformation in ductile single crystals. Acta Metall 1982;30(6):1087–119. http://dx.doi.org/10.1016/0001-6160(82)90005-0.

[60] Peirce D, Asaro RJ, Needleman A. Material rate dependence and localized deformation in crystalline solids. Acta Metall 1983;31(12):1951–76. http://dx.doi.org/10.1016/0001-6160(83)90014-7.

[61] Lee EH. Elastic-plastic deformation at finite strains. J Appl Mech 1969;36(1):1–6. http://dx.doi.org/10.1115/1.3564580.

[62] Frederick CO, Armstrong PJ. A mathematical representation of the multiaxial Bauschinger effect. Mater High Temp 1966;24(1):1–26. http://dx.doi.org/10.3184/096034007x207589, URL https://hdl.handle.net/2381/40272.

[63] Dunne F, Wilkinson AJ, Allen R. Experimental and computational studies of low cycle fatigue crack nucleation in a polycrystal. Int J Plast 2007;23(2):273–95. http://dx.doi.org/10.1016/j.ijplas.2006.07.001.

[64] Natkowski E, Durmaz AR, Sonnweber-Ribic P, Münstermann S. Fatigue lifetime prediction with a validated micromechanical short crack model for the ferritic steel EN 1.4003. Int J Fatigue 2021;152:106418. http://dx.doi.org/10.1016/j.ijfatigue.2021.106418.

[65] Sharaf M, Kucharczyk P, Vajragupta N, Münstermann S, Hartmaier A, Bleck W. Modeling the microstructure influence on fatigue life variability in structural steels. Comput Mater Sci 2014;94:258–72. http://dx.doi.org/10.1016/j.commatsci.2014.05.059.

[66] Skelton R. Energy criteria and cumulative damage during fatigue crack growth. Int J Fatigue 1998;20(9):641–9. http://dx.doi.org/10.1016/S0142-1123(98)00027-9.

[67] Charkaluk E, Constantinescu A. An energetic approach in thermomechanical fatigue for silicon molybdenum cast iron. Mater High Temp 2000;17(3):373–80. http://dx.doi.org/10.1179/mht.2000.17.3.001.

[68] Korsunsky AM, Dini D, Dunne FP, Walsh MJ. Comparative assessment of dissipated energy and other fatigue criteria. Int J Fatigue 2007;29(9–11):1990–5. http://dx.doi.org/10.1016/j.ijfatigue.2007.01.007.

[69] Boeff M. Micromechanical modelling of fatigue crack initiation and growth [Ph.D. thesis], Bochum, Germany: Ruhr University Bochum; 2016.
[70] Shenoy M, Zhang J, McDowell DL. Estimating fatigue sensitivity to polycrystalline Ni-base superalloy microstructures using a computational approach. Fatigue Fract Eng Mat Struct 2007;30(10):889–904. http://dx.doi.org/10.1111/j.1460-2695.2007.01159.x.
[71] Gillner K, Münstermann S. Numerically predicted high cycle fatigue properties through representative volume elements of the microstructure. Int J Fatigue 2017;105:219–34. http://dx.doi.org/10.1016/j.ijfatigue.2017.09.002.
[72] Schoenborn S, Kaufmann H, Sonsino CM, Heim R. Variable amplitude fatigue of high-strength cast iron alloys for automotive applications. Int J Fatigue 2016;91:445–58. http://dx.doi.org/10.1016/j.ijfatigue.2016.01.006.
[73] Castelluccio GM. A study on the influence of microstructure on small fatigue cracks [Ph.D. thesis], Georgia, Atlanta, USA: Georgia Institute of Technology; 2012.
[74] Tsuzaki K, Nakanishi E, Maki T, Tamura I. Low-cycle fatigue behavior in metastable austenitic steel accompanying deformation-induced martensitic transformation. Trans Iron Steel Inst Jpn 1983;23(10):834–41. http://dx.doi.org/10.2355/isijinternational1966.23.834.
[75] Talonen J, Aspegren P, Hänninen H. Comparison of different methods for measuring strain induced α-martensite content in austenitic steels. Mater Sci Technol 2004;20(12):1506–12. http://dx.doi.org/10.1179/026708304X4367.
[76] Schäfer BJ, Song X, Sonnweber-Ribic P, ul Hassan H, Hartmaier A. Micromechanical modelling of the cyclic deformation behavior of martensitic SAE 4150 – a comparison of different kinematic hardening models. Metals 2019;9(3):368. http://dx.doi.org/10.3390/met9030368.
[77] Lee M-G, Kim S-J, Han HN. Crystal plasticity finite element modeling of mechanically induced martensitic transformation (MIMT) in metastable austenite. Int J Plast 2010;26(5):688–710. http://dx.doi.org/10.1016/j.ijplas.2009.10.001.
[78] Ma A, Hartmaier A. A study of deformation and phase transformation coupling for TRIP-assisted steels. Int J Plast 2015;64:40–55. http://dx.doi.org/10.1016/j.ijplas.2014.07.008.
[79] Shahmardani M, Logvinov R, Babinský T, Guth S, Paul S, Biswas A, Vajragupta N, Hartmaier A. Experimental assessment and micromechanical modeling of additively manufactured austenitic steels under cyclic loading. Adv Eng Mater 2023;25(15). http://dx.doi.org/10.1002/adem.202300103.
[80] Morrow J. Cyclic plastic strain energy and fatigue of metals. In: Lazan BJ, editor. Internal friction, damping, and cyclic plasticity. ASTM International; 1965, p. 45–87. http://dx.doi.org/10.1520/STP43764S.
[81] Fatemi A, Socie DF. A critical plane approach to multiaxial fatigue damage including out-of-phase loading. Fatigue Fract Eng Mat Struct 1988;11(3):149–65. http://dx.doi.org/10.1111/j.1460-2695.1988.tb01169.x.
[82] Castelluccio GM, McDowell DL. Effect of annealing twins on crack initiation under high cycle fatigue conditions. J Mater Sci 2013;48(6):2376–87. http://dx.doi.org/10.1007/s10853-012-7021-y.
[83] Schäfer BJ, Sonnweber-Ribic P, ul Hassan H, Hartmaier A. Micromechanical modelling of the influence of strain ratio on fatigue crack initiation in a martensitic steel – a comparison of different fatigue indicator parameters. Materials 2019;12(18). http://dx.doi.org/10.3390/ma12182852.
[84] Zinovev A. Crystal plasticity modelling of thermomechanical fatigue in ITER relevant tungsten [Ph.D. thesis], Louvain-la-Neuve, Belgium: Université Catholique de Louvain, Ecole Polytechnique de Louvain; 2019.
[85] Antolovich SD, Singh B. On the toughness increment associated with the austenite to martensite phase transformation in TRIP steels. Met Trans 1971;2(8):2135–41. http://dx.doi.org/10.1007/BF02917542.
[86] Hennessy D, Steckel G, Altstetter C. Phase transformation of stainless steel during fatigue. Metall Trans A 1976;7(3):415–24. http://dx.doi.org/10.1007/BF02642838.
[87] Wang X, Liu C, Sun B, Ponge D, Jiang C, Raabe D. The dual role of martensitic transformation in fatigue crack growth. Proc Natl Acad Sci USA 2022;119(9). http://dx.doi.org/10.1073/pnas.2110139119.
[88] Gupta S, Ma A, Hartmaier A. Mechanical twinning induced alteration in the kinetics of martensitic phase transformation in TRIP-maraging steels. Int J Solids Struct 2018;155:213–24. http://dx.doi.org/10.1016/j.ijsolstr.2018.07.021.
[89] Moore JA, Rusch JP, Nezhad PS, Manchiraju S, Erdeniz D. Effects of martensitic phase transformation on fatigue indicator parameters determined by a crystal plasticity model. Int J Fatigue 2023;168:107457. http://dx.doi.org/10.1016/j.ijfatigue.2022.107457.